

# UC Berkeley

## UC Berkeley Previously Published Works

### Title

Uncertainties in Atmospheric River Life Cycles by Detection Algorithms: Climatology and Variability

### Permalink

<https://escholarship.org/uc/item/44g4w45z>

### Authors

Zhou, Yang  
O'Brien, Travis  
Ullrich, Paul  
[et al.](#)

### Publication Date

2020-09-16

### DOI

10.1002/essoar.10504174.1

Peer reviewed

# Lawrence Berkeley National Laboratory

## Recent Work

### Title

Uncertainties in Atmospheric River Lifecycles by Detection Algorithms: Climatology and Variability

### Permalink

<https://escholarship.org/uc/item/7b38c508>

### Journal

Journal of Geophysical Research: Atmospheres, 126(8)

### ISSN

2169-897X

### Authors

Zhou, Y  
O'Brien, TA  
Ullrich, PA  
[et al.](#)

### Publication Date

2021-04-01

### DOI

10.1029/2020JD033711

Peer reviewed



23  
24  
25  
26  
27  
28  
29  
30  
31  
32  
33  
34  
35  
36  
37  
38  
39  
40  
41  
42  
43

**Abstract**

Atmospheric rivers (ARs) are long and narrow filaments of vapor transport responsible for most poleward moisture transport outside of the tropics. Many AR detection algorithms have been developed to automatically identify ARs in climate data. The diversity of these algorithms has introduced appreciable uncertainties in quantitative measures of AR properties and thereby impedes the construction of a unified and internally consistent climatology of ARs. This paper compares eight global AR detection algorithms from the perspective of AR life cycles following the propagation of ARs from origin to termination in the MERRA2 reanalysis over the period 1980-2017. Uncertainties related to lifecycle characteristics, including number, lifetime, intensity, and frequency distribution are discussed. Notably, the number of AR events per year in the Northern Hemisphere can vary by a factor of 5 with different algorithms. Although all algorithms show that the maximum origin (termination) frequency locates over the northwestern (northeastern) Pacific, significant disagreements occur in regional distribution. Spreads are large in AR lifetime and intensity. The number of landfalling AR events produced by the algorithms can vary from 16 to 78 events per cool season, i.e. by almost a factor of five, although the agreement improves for stronger ARs. By examining the AR's connection with the Madden-Julian Oscillation and El Niño Southern Oscillation, we find that the overall responses of ARs (such as changes in AR frequency, origin, and landfalling activity) to low-frequency climate variabilities are consistent among algorithms.

44  
45  
46  
47  
48  
49  
50  
51  
52  
53  
54  
55  
56  
57  
58  
59

### **Plain Language Summary**

Atmospheric rivers (ARs) are strong moisture transport in the atmosphere that is one of the dominant processes conveying water vapor from the tropics to high latitudes. ARs are also important water sources to coastal regions like the west coast of North America. Many studies have developed their own detection algorithms to study ARs. However, conclusions from these studies may differ because of different algorithm designs. Here we select an ensemble of eight detection algorithms and analyze the disagreement in AR characteristics across the ensemble including AR size, number, lifetime, intensity, and landfalling activity applied to a single dataset describing meteorological conditions in the recent past. Results suggest that basic AR characteristics vary significantly depending on the detection algorithm. Meanwhile, the large spread may be smoothed out when examining AR behavior in the intraseasonal and interannual time scale.

## 60 **1. Introduction**

61 Atmospheric rivers (ARs) are meteorological phenomena with a long and narrow  
62 filamentary structure of poleward moisture transport outside of the tropics. ARs are essential to  
63 the global hydrological cycle and are often linked to weather and climate extremes (Newell et al.,  
64 1992; Zhu & Newell, 1994). Due to their crucial role in water resources (Dettinger, 2013; Dettinger  
65 et al., 2011; Gorodetskaya et al., 2014) and their hydrological impacts of heavy precipitation and  
66 flooding (Lavers et al., 2011; Lavers et al., 2014; Neiman et al., 2013; Neiman et al., 2008; Ralph  
67 et al., 2006; Waliser & Guan, 2017), numerous studies have extensively investigated different  
68 aspects of ARs in the past two decades, including landfalling activity (Hu et al., 2017; Rutz et al.,  
69 2014), connections with low-frequency modes of climate variability (Gershunov et al., 2017; Guan  
70 & Waliser, 2015; Kim et al., 2017; Mundhenk et al., 2016; Payne & Magnusdottir, 2014),  
71 subseasonal-to-seasonal prediction (DeFlorio, Waliser, Guan, Lavers, et al., 2018; DeFlorio,  
72 Waliser, Guan, Ralph, et al., 2018; Lavers et al., 2014; Zhou & Kim, 2017), and future projections  
73 (Lavers et al., 2013; Payne & Magnusdottir, 2015; Radic et al., 2015; Shields & Kiehl, 2016b).

74 The American Meteorological Society (AMS) Glossary of Meteorology qualitatively  
75 defines an AR as “a long, narrow, and transient corridor of strong horizontal water vapor transport  
76 that is typically associated with a low-level jet stream ahead of the cold front of an extratropical  
77 cyclone”, with no extant quantitative definition. Therefore, a great diversity of AR detection  
78 algorithms has emerged from research groups targeting different scientific questions. For example,  
79 in order to measure the impacts of AR’s in-land penetration over North America, Rutz et al. (2014)  
80 defines an AR as regions where the magnitude of vertically-integrated moisture flux (IVT) exceeds  
81  $250 \text{ kg m}^{-1} \text{ s}^{-1}$  with lengths longer than 2000 km. Likewise, to understand global AR activity, Guan  
82 and Waliser (2015) defines an AR by applying a relative threshold on IVT (exceeding 85<sup>th</sup>

83 percentile) that varies spatially with other criteria on geometric shapes. However, the variety of  
84 AR detection algorithms introduces uncertainties in AR measures and understanding of AR  
85 activity. For example, Huning et al. (2017) show a 20% difference in ARs contribution to seasonal  
86 cumulative snowfall over the Sierra Nevada when using an IVT-based versus integrated water  
87 vapor (IWV)-based definition. To quantify and understand uncertainties that arise from different  
88 AR detection algorithms, the Atmospheric River Tracking Method Intercomparison Project  
89 (ARTMIP) was formed as an ad hoc, international collaboration (Shields et al., 2018). ARTMIP  
90 includes over 30 (and growing) AR detection algorithms and is dedicated to providing guidance  
91 on the most suitable algorithms for particular scientific applications. Ralph et al. (2018)  
92 investigates ARs that made landfall in northern California using outputs from 10 AR detection  
93 algorithms and concludes that the number of ARs can vary by a factor of two across this  
94 representative set of algorithms. By examining the role of ARs in the western US watershed, Chen  
95 et al. (2019) compares six detection algorithms and shows that the major difference from detection  
96 algorithms is the precipitation amount, while the temperature changes in AR events are consistent  
97 among algorithms. The ranges in AR climatological properties, including landfalling frequency  
98 and duration, as well as seasonality, arising from the differences among ARs identified using 19  
99 detection algorithms have been discussed in detail in Rutz et al. (2019).

100         These studies mainly focus on uncertainties in landfalling AR activity and related  
101 hydrological impacts. Uncertainties in measures of AR origination and evolution over the ocean,  
102 including frequency and propagation before landfall, have not been well-documented. Thus, in the  
103 framework of ARTMIP, the goal of the present study is to understand uncertainties in ARs  
104 stemming from detection algorithms within the context of AR life cycles. The life cycle of an AR  
105 event records the complete propagation of AR-associated moisture transport from its origin to

106 termination. To track ARs spatiotemporally, an object-based automated AR tracking algorithm has  
107 been developed in Zhou et al. (2018) that can assemble the AR life cycles from the single time-  
108 level masks produces by different detection algorithms. With this tool in hand, we will address  
109 two questions: (1) To what degree are AR lifecycle characteristics (number, lifetime, intensity,  
110 and distributions of AR origin and termination) sensitive to the choice of AR detection algorithms?  
111 (2) Are the correlations between AR life cycles and various modes of climate variability (such as  
112 the Madden-Julian Oscillation (MJO) and El Niño Southern Oscillation (ENSO)) robust to the  
113 choice of detection algorithms? This study will be the first to apply a common tracking method  
114 across various AR detection algorithms and examine the associated uncertainties. It also provides  
115 a benchmark for AR life cycle sensitivities across detection algorithms. Further, this study has  
116 implications for improving prediction of AR activity by providing the degree of agreements among  
117 detection algorithms based on AR intensities and for reducing uncertainties in AR changes in the  
118 future climate by accessing the potentially well-suited algorithms in the context of projected AR  
119 life cycles.

120 In section 2, the AR detection algorithms selected from ARTMIP and the Zhou et al. (2018)  
121 AR life cycle tracking algorithm are introduced. Uncertainties in lifecycle characteristics are  
122 discussed in section 3. In sections 4 and 5 we investigate the sensitivity of AR connections with  
123 the MJO and ENSO respectively. Summary and discussion are provided in section 6.

124

## 125 **2. Data and methods**

### 126 2.1 Tracking AR life cycles from different detection algorithms

127 To investigate the uncertainty in AR life cycle stemming from detection algorithms, we  
128 use 15 of the global AR detection algorithms from the ARTMIP Tier 1 collection (Table 1) that



129 were available at the time of analysis. A more detailed description of participating ARTMIP Tier  
130 1 algorithms and AR catalogues are provided in Shields et al. (2018). In ARTMIP Tier1, all  
131 participants apply their algorithms to the 3-hourly 0.5-degree latitude by 0.625-degree longitude  
132 Modern Era Retrospective analysis for Research and Applications, version 2 (MERRA2)  
133 reanalysis from 1980-2017 (Gelaro et al., 2017). Note that some algorithms can be tuned for  
134 particular scientific applications (such as Tempest), the included algorithms in this study are in  
135 their default settings. As shown in Table 1, each algorithm has different thresholds on IVT or IWV  
136 to detect ARs. There are two major kinds of thresholds: absolute thresholds specified by spatially  
137 and temporally invariant values (e.g. AR-CONNECT and Rutz), and relative thresholds specified  
138 by fixed percentiles of spatiotemporal varying IVT or IWV (e.g. Guan\_Waliser and Lora\_global).  
139 Additional thresholds frequently employed by detection algorithms include geometric constraints  
140 and machine learning techniques (e.g. TECA\_bard\_v1). We further largely focus our analysis on  
141 the Northern Hemisphere.

142 We adopt the automated tracking algorithm developed by Zhou and Kim (2019); Zhou et  
143 al. (2018) to identify the life cycle of AR events. The term “detection” and “tracking” are  
144 sometimes used interchangeably by previous literature to describe AR identification. In this study,  
145 we use “detection” for recognition of instantaneous AR conditions (i.e. AR objects, explained later)  
146 and “tracking” for spatiotemporally tracing the life cycle of AR events. Therefore, we refer to the  
147 selected ARTMIP algorithms as AR “detection” algorithms and the Zhou et al. (2018) algorithm  
148 as the “tracking” algorithm. We define an AR object as an enclosed two-dimensional (latitude and  
149 longitude) instantaneous area that meets the criteria of AR conditions. The life cycle of an AR  
150 event is tracked by connecting the spatiotemporal overlapping AR objects (more details in section  
151 3) from origin to termination.

## 152 2.2 Climate variability indices

153 We investigate the robustness of the relationships between ARs and low-frequency climate  
154 variabilities with a focus on the MJO and ENSO. The Real-time Multivariate MJO index (RMM,  
155 (Wheeler & Hendon, 2004)) is obtained to describe the MJO phase and amplitude. The MJO is  
156 distinguished into eight phases depending on the location of enhanced convection using two RMM  
157 components (Supplemental Figure S1). We define an MJO day when the RMM amplitude  
158 ( $\sqrt{\text{RMM1}^2 + \text{RMM2}^2}$ ) exceeds 1.0. We use daily interpolated 20-100-day-filtered outgoing  
159 longwave radiation (OLR) (Liebmann & Smith, 1996) to indicate the location of MJO convection.

160 We use the ENSO Longitude Index (ELI, Williams and Patricola (2018)) to identify El  
161 Niño and La Niña events. The ELI index is an SST-based metric that captures the average  
162 longitude of Pacific tropical deep convection. We used ELI because it is able to characterize the  
163 diversity of ENSO events in a single index (Williams & Patricola, 2018) and because it better  
164 describes seasonal variations in western U.S. winter precipitation compared with other ENSO  
165 indices (Patricola et al., 2020). For each month, the ELI index is calculated by first averaging the  
166 sea surface temperature between 5°S-5°N. Next, a binary mask is created where equatorial  
167 gridpoints with meridionally-averaged-SST exceeding the convection threshold (tropics-wide  
168 averaged SST) are assigned a value of 1 and otherwise 0. Finally, the ELI index is the average of  
169 longitudes of all the equatorial gridpoints with masks equaling 1. The ELI index is constructed  
170 using monthly 2-degree Extended Reconstructed SST v5 (Huang et al., 2017) from December to  
171 February from 1980-2016. The ENSO event is categorized by the absolute value of the ELI index.  
172 We select the El Niño and La Niña years following the years of moderate and strong ENSO events  
173 in Patricola et al. (2020) (in their Table 1). The same analysis is conducted with Niño 3.4 index  
174 and SOI index and the results are consistent with the ELI index (not shown).

Acronyms	Reference	Type	Detection thresholds	Region
*AR-CONNECT	Shearer et al. (2020)	Track	IVT = 300 kg m <sup>-1</sup> s <sup>-1</sup> , time-stitching for minimum 24 hours	Global
CONNECT500	Sellars et al. (2015); Sellars et al. (2013)	Track	IVT = 500 kg m <sup>-1</sup> s <sup>-1</sup>	Global
CONNECT700			IVT = 700 kg m <sup>-1</sup> s <sup>-1</sup>	
*TECA_bard_v1	O'Brien et al. (2020)	Condition	Relative threshold (based on spatial percentile for each timestep). An inverted Gaussian filter is applied at the equator to damp out the ITCZ	Global
Cascade_ivt	Experimental	Condition	Convolutional neural network to replicate ARTMIP mean; Threshold free; use IVT as input	Global
Cascade_iwv			Same as above, but use IWV as input	Global
*Guan_Waliser	Guan and Waliser (2015)	Condition	85 <sup>th</sup> percentile IVT; Absolute minimum requirement designed for polar locations: 100 kg m <sup>-1</sup> s <sup>-1</sup> IVT	Global
*Mundhenk_v3	Mundhenk et al. (2016)	Condition	IVT percentiles and/or anomalies both temporal and spatial	Global
Rutz	Rutz et al. (2014)	Condition	IVT (surface to 100mb) = 250 kg m <sup>-1</sup> s <sup>-1</sup>	Global
Sail_v1	Project: Atmospheric rivers identification, tracking and climatology assessment	Condition	80 <sup>th</sup> percentile IVT; length-width ratio exceeds 5	Global
*Lora_global	Lora et al. (2017)	Condition	Length >= 2000km; IVT 100kgm <sup>-1</sup> s <sup>-1</sup> above climatological area means for the North Pacific	Global
*Lora_v2			Length >= 2000km; Relative to 30-day running mean of background IWV	Global
Tempest_ivt250	Rhoades et al. (2020);	Track	$\nabla^2$ IVT <= -4e4 kg m <sup>-1</sup> s <sup>-1</sup> rad <sup>-2</sup> , IVT >=250 kg m <sup>-1</sup> s <sup>-1</sup>	Global, latitude ≥15°
*Tempest_ivt500	McClenny et al. (2020)		$\nabla^2$ IVT <= -4e4 kg m <sup>-1</sup> s <sup>-1</sup> rad <sup>-2</sup> , IVT >=500 kg m <sup>-1</sup> s <sup>-1</sup>	
*Tempest_ivt700			$\nabla^2$ IVT <= -4e4 kg m <sup>-1</sup> s <sup>-1</sup> rad <sup>-2</sup> , IVT >=700 kg m <sup>-1</sup> s <sup>-1</sup>	

175 Table 1. List of selected AR detection algorithms. More information is listed on  
 176 <http://www.cgd.ucar.edu/projects/artmip/algorithms.html>. Algorithms marked with asterisk are adopted for extended analysis.

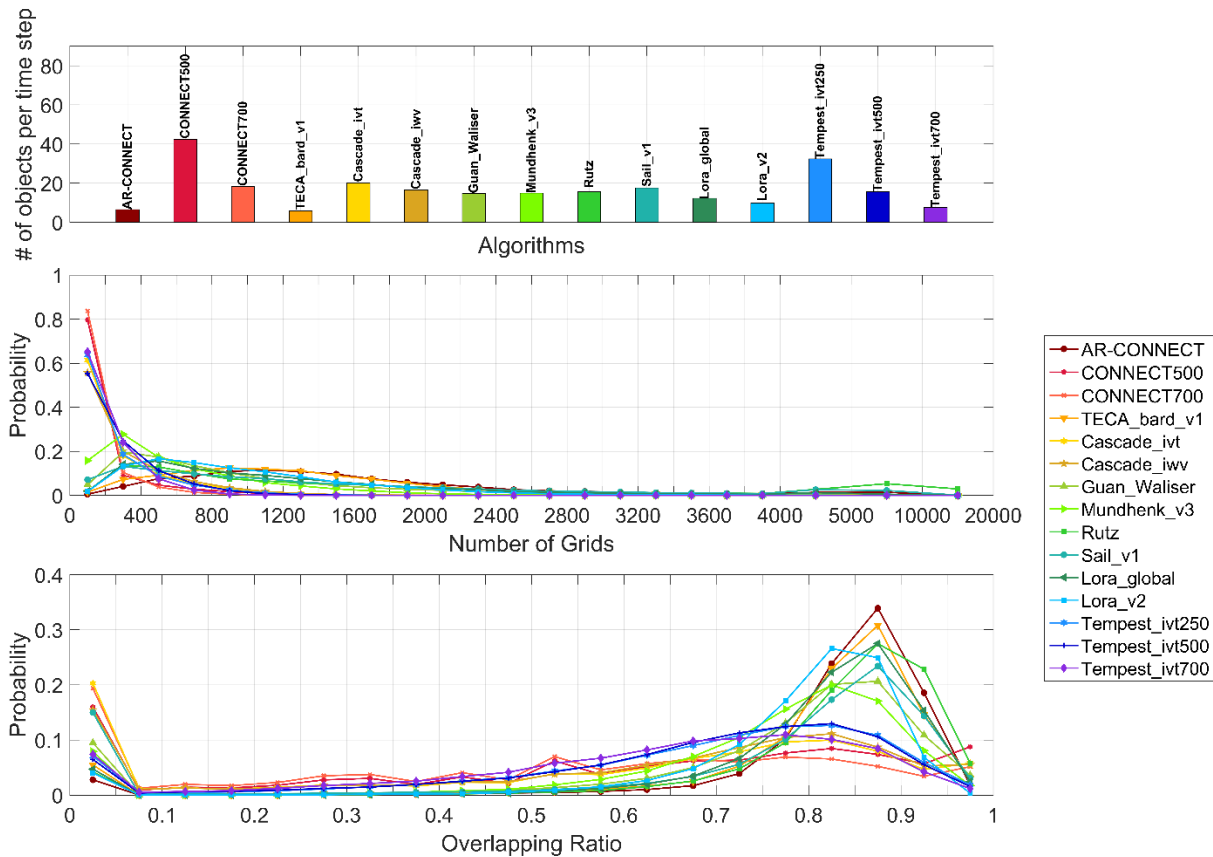
177

178 **3. Life-cycle characteristics**

179 Figure 1 shows the distributions of number, size, and overlapping ratio of AR objects  
180 identified by 15 detection algorithms using global 3-hourly AR objects from the year 2016 (total  
181 of 2928 time steps). We arbitrarily select the year 2016 to examine the characteristics of AR objects.  
182 The average number of objects per time step varies from 6 to 42 (Figure 1a), where the lowest  
183 number is from TECA\_bard\_v1 which includes a set of “plausible” AR detectors and the highest  
184 number is from CONNECT500 which captures some tropical disturbances that may not be  
185 associated with ARs or are entrained by ARs over their life cycle (e.g., tropical cyclones) (not  
186 shown). About 10 algorithms detect 10-20 global AR objects at any given time step, which is  
187 consistent with the number from a manual analysis by Newell et al. (1992) and the number range  
188 of expert-identified global AR objects (O'Brien et al., 2020).

189 The probability distributions of object size and overlapping ratio vary among algorithms  
190 (Figure 1b-c). The object size is represented by the number of gridpoints ( $0.5^\circ \times 0.625^\circ$ ) within an  
191 object. The overlapping ratio is a key parameter in the tracking algorithm, which is calculated as  
192 the ratio of overlapping area with the object at previous time step  $t-1$  to the total area of object at  $t$   
193 (Zhou et al., 2018). A zero overlapping ratio of an object indicates the origin of an AR event.  
194 Figures 1b-c suggest two types of distribution curves. The first type demonstrates a higher  
195 percentage of smaller objects (less than 800 gridpoints) with a wider spread in overlapping ratio,  
196 which may be due to identification of non-AR tropical disturbances that are usually smaller in size  
197 (such as CONNECT500 and CONNECT700); or recognition of an IVT core that is smaller in size  
198 (such as the Tempest family). The Cascade\_iwv and Cascade\_ivt algorithms determine an AR  
199 object based on a machine learning algorithm trained on the consensus of all ARTMIP algorithms,

200 which makes them prone to identify primarily the IVT core, resulting in relatively smaller AR  
 201 objects. Algorithms showing the second type of distribution curve mostly capture the general long  
 202 and narrow shape of ARs (wider spread in object size) and present higher spatiotemporal  
 203 connectivity with more than 80% of overlapping ratio exceeding 0.7. However, some algorithms  
 204 detect objects with more than 5000 gridpoints (such as Rutz and Sail\_v1), which may include the  
 205 Inter Tropical Convergence Zone (ITCZ). To exclude the impacts from ITCZ and tropical  
 206 disturbances, we narrow the selected algorithms down to eight algorithms for further analysis  
 207 (Table 1, marked with asterisks).



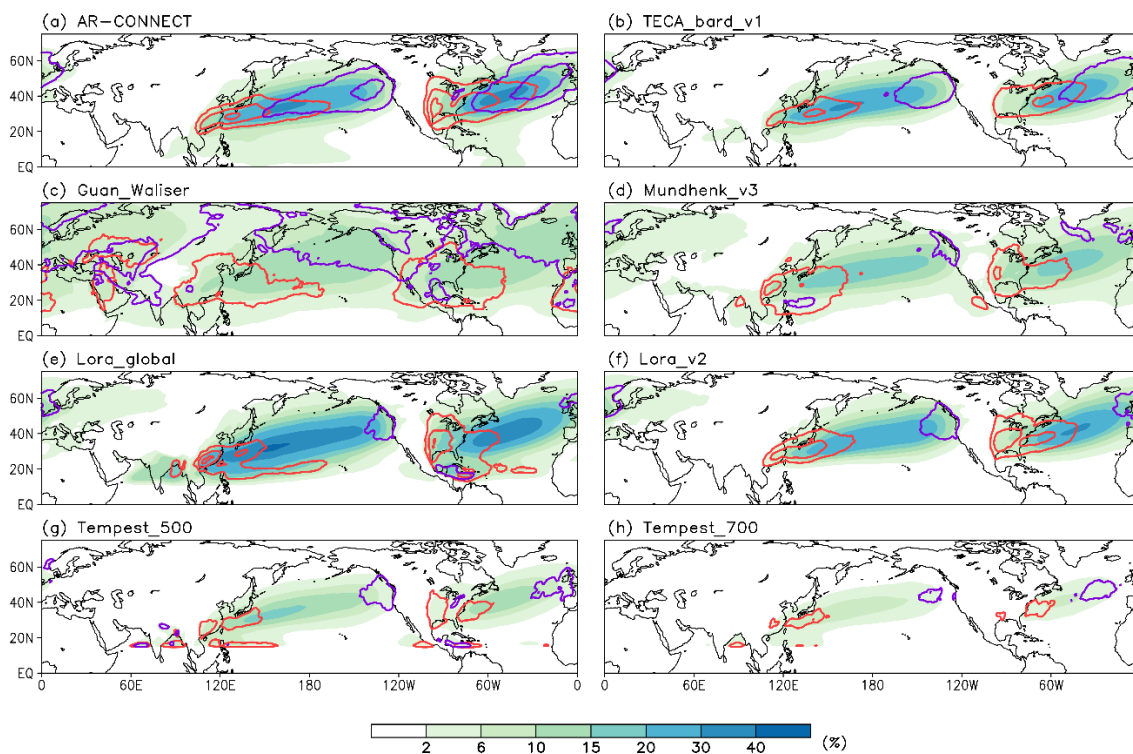
208  
 209 Figure 1. (a) Average number of global AR objects per time step. Probability distribution of (b)  
 210 object sizes and (c) overlapping ratio. Data: 3-hourly AR objects from the year 2016.

211

## 212 3.1 Climatology

213 Variations in the number and size of AR objects are reflected in the annual mean AR  
214 frequency (Figure 2). The AR frequency is calculated as, for each year, the gridpoint-accumulated  
215 number of AR objects normalized by the number of time steps (unit: percent of time steps). All  
216 algorithms show that in the Northern Hemisphere, high AR frequency appears over the ocean basin,  
217 where regions between 20°N-40°N are impacted by AR conditions about 10-30% of the time. AR  
218 frequency over the northwestern ocean basin is generally higher than that over the northeastern  
219 ocean basins. Due to higher IVT thresholds, the Tempest family naturally detects smaller AR  
220 objects and therefore shows a weaker amplitude of AR frequency (Figure 2g-h).

221 The origin (termination) object is defined as the first (last) object of an AR life cycle. The  
222 overall distribution of origin frequency is consistent among algorithms, with the maximum over  
223 the northwestern ocean between 20°N-40°N, which may be associated with more moisture by  
224 warmer sea surface temperature and more tropical cyclones. The disagreement between algorithms  
225 lies in the amplitude and regional distribution which are largely affected by the choice of threshold.  
226 The maximum termination frequency is concentrated over the eastern ocean and the west coast of  
227 North America and Europe. The termination frequency spreads more broadly in Guan\_Waliser  
228 because more inland-penetrating AR activity being captured. Guan\_Waliser also detects moisture  
229 transport activity over western Asia and the Arabian Peninsula, which may be linked to Somali Jet  
230 (Halpern & Woiceshyn, 1999). Overall, algorithms show agreement in the distributions of AR  
231 total, origin, and termination frequency. However, the uncertainties from algorithms may be large  
232 when it comes to regional studies, such as estimating the hydrological impacts from landfalling  
233 ARs (Rutz et al., 2019; Shields et al., 2018).



234  
 235 Figure 2. Annual mean total AR frequency (shading), origin (red contour), and termination  
 236 frequencies (violet contour). Unit is percent of time steps. Note that shading intervals are not  
 237 constant. Contour interval: (a-f) 0.2 percent of time steps and (g-h) 0.1 percent of time steps, zero  
 238 lines are omitted.

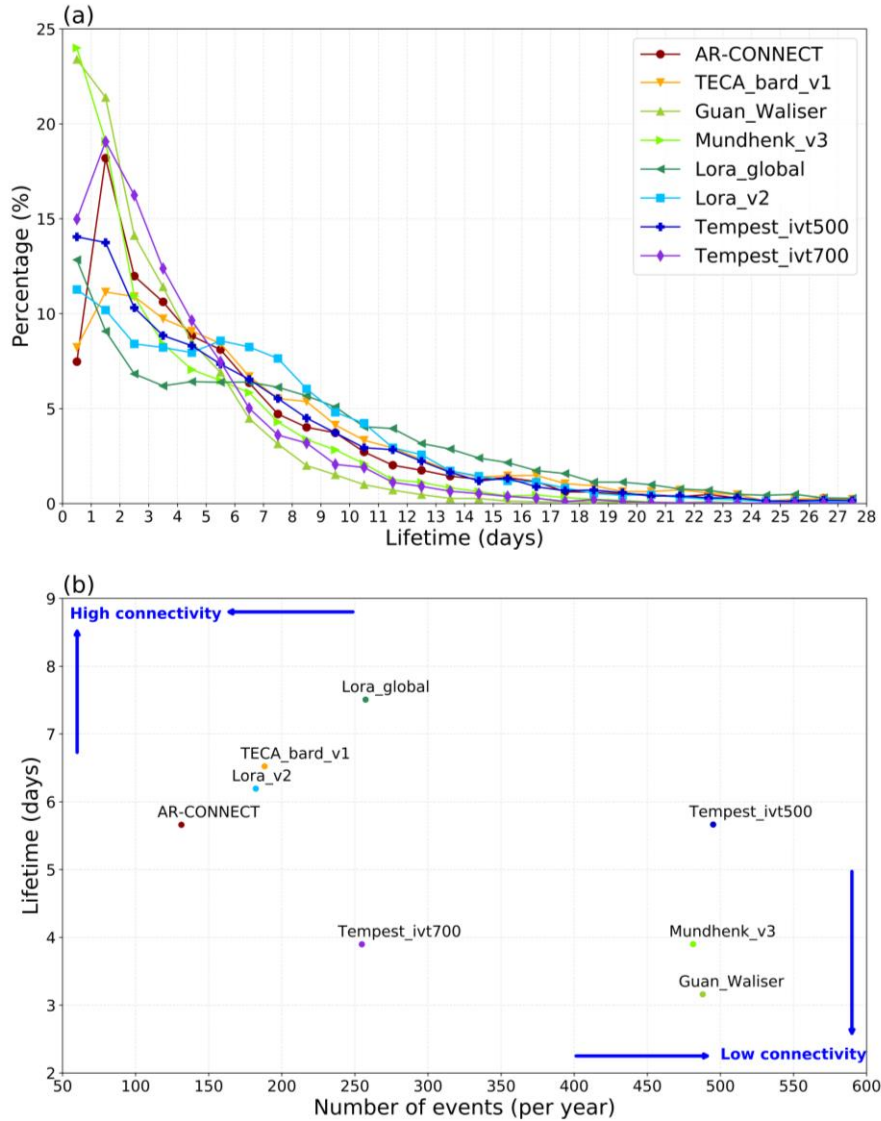
239  
 240 The lifetime of an AR event represents how long an event lasts, which is calculated as the  
 241 number of time intervals within the life cycle multiplied by the time interval (3 hours). All  
 242 algorithms show that about 40-50% of North Pacific ARs (originated between 100°E-240°E) last  
 243 less than 4 days (Figure 3a). About 40% of ARs detected by Guan\_Waliser and Mundhenk\_v3 last  
 244 less than 2 days, which may be due to that one complete AR life cycle is identified as multiple life  
 245 cycle pieces with shorter lifetimes because of some missing objects by these algorithms. This is  
 246 reflected in Figure 3b which indicates the spatiotemporal connectivity by showing the mean AR  
 247 lifetime and the annual number of North Pacific AR events. Algorithms closer to the lower right

248 corner suggest a relatively lower spatiotemporal connectivity – with a similar number range of AR  
249 objects per time step (Figure 1a), a greater number of AR events with shorter lifetime implies a  
250 higher chance of discontinuous life cycles. Algorithms closer to the upper left corner indicate  
251 higher spatiotemporal connectivity. These algorithms have more concentrated distributions of  
252 origin and termination frequency (Figure 2), suggesting more AR events originate over the  
253 northwestern Pacific, travel across the ocean, and terminate over the northeastern Pacific. The  
254 distribution of North Atlantic AR lifetimes is similar to that of the North Pacific ARs  
255 (Supplemental Figure S2). On average, North Atlantic ARs last one day shorter than the North  
256 Pacific ARs in most algorithms, which is mostly due to the shorter travel distance in the North  
257 Atlantic basin comparing with that in the North Pacific (Supplemental Figure S3). The travel  
258 distance of an AR event represents how long an AR event propagates during its life cycle, which  
259 shows a positive correlation with AR lifetime. The mean travel distance of North Pacific ARs can  
260 range from  $5 \times 10^3$  km (Tempest\_ivt700) to  $15 \times 10^3$  km (Lora\_v2). Generally, algorithms suggest  
261 that more than 80% of North Pacific and North Atlantic ARs travels within  $25 \times 10^3$  km  
262 (Supplemental Figure S3).

263         The propagation speed is calculated by dividing the travel distance with AR lifetime, which  
264 shows how fast an IVT centroid travels during the life cycle (Figure 4a). The location of IVT  
265 centroid is determined by the mass-weighted averaged longitude and latitude within an object.  
266 Therefore, the propagation speed is impacted by the geometric consistency of AR objects in a life  
267 cycle – a sudden deformation of objects between two consecutive time steps can result in a spurious  
268 change in propagation speed. The Tempest family consistently detects the IVT core, which shows  
269 the most concentratedly distributed propagation speed with an average of about 59 km/hr. Other  
270 algorithms, with a broader range in object sizes (Figure 1b), present wider spread in propagation



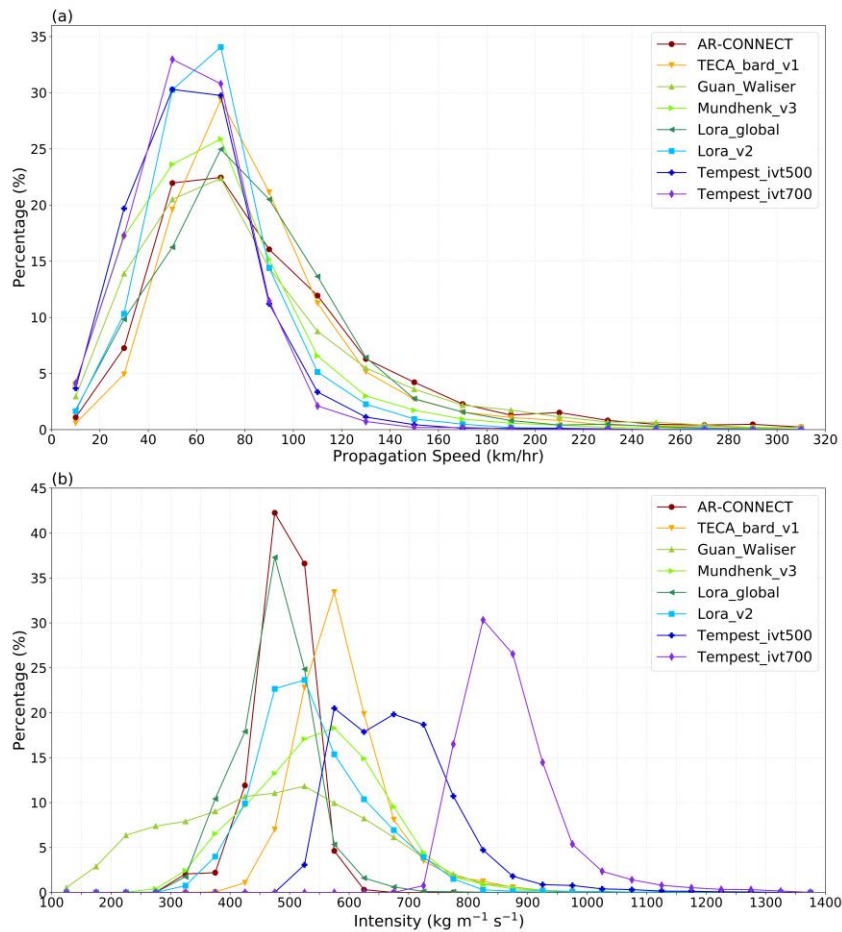
271 speeds with averages ranging from 70-90 km/hr. Nearly identical distribution is shown with North  
 272 Atlantic ARs (Supplemental Figure S4a).



273  
 274 Figure 3. (a) Percentage distribution of North Pacific AR lifetime. (b) Scatter plot of the number  
 275 of North Pacific AR events per year and their mean lifetime.

276  
 277 The lifecycle intensity is calculated as the mean of domain averaged IVT magnitude ( $|IVT|$ )  
 278 within AR objects in the life cycle. Most algorithms detect lifecycle intensity in the range of 300-  
 279 800  $\text{kg m}^{-1} \text{s}^{-1}$  (Figure 4b). Variations within this range can be due to subtle inconsistencies in the

280 binary masks of AR objects; wider (narrower) objects will tend to sweep up more points with  
 281 lower (higher) IVT values. Guan\_Waliser shows the largest spread in lifecycle intensity because  
 282 their relative percentile threshold includes objects over land and the polar regions which possess  
 283 weaker |IVT|. Spread is smaller in AR-CONNECT, Lora\_global, and TECA\_bard\_v1. The  
 284 lifecycle intensities of Tempest\_ivt500 and Tempest\_ivt700 are much stronger than other  
 285 algorithms. The lifecycle intensity of North Atlantic ARs shows a similar distribution as the North  
 286 Pacific ARs but with a smaller spread in most algorithms (Supplemental Figure S4b).



287  
 288 Figure 4. Distribution of (a) propagation speed (km/hour) and (b) lifecycle intensity ( $\text{kg m}^{-1} \text{s}^{-1}$ )  
 289 for North Pacific AR events.

290

291 By comparing the number, lifetime, travel distance, propagation speed, and lifecycle  
292 intensity of AR events, we find that detection algorithms can introduce uncertainties in  
293 understanding the life cycle of AR events. The spatiotemporal connectivity plays a crucial role in  
294 determining the number and lifetime of AR events, and can further affect the distribution of AR  
295 origins and terminations, which can be problematic for examinations on AR's dynamical processes.  
296 The spread in lifecycle intensity may raise uncertainties in quantifying AR's contribution to the  
297 global hydrological cycle.

### 298 3.2 Landfalling ARs over North America

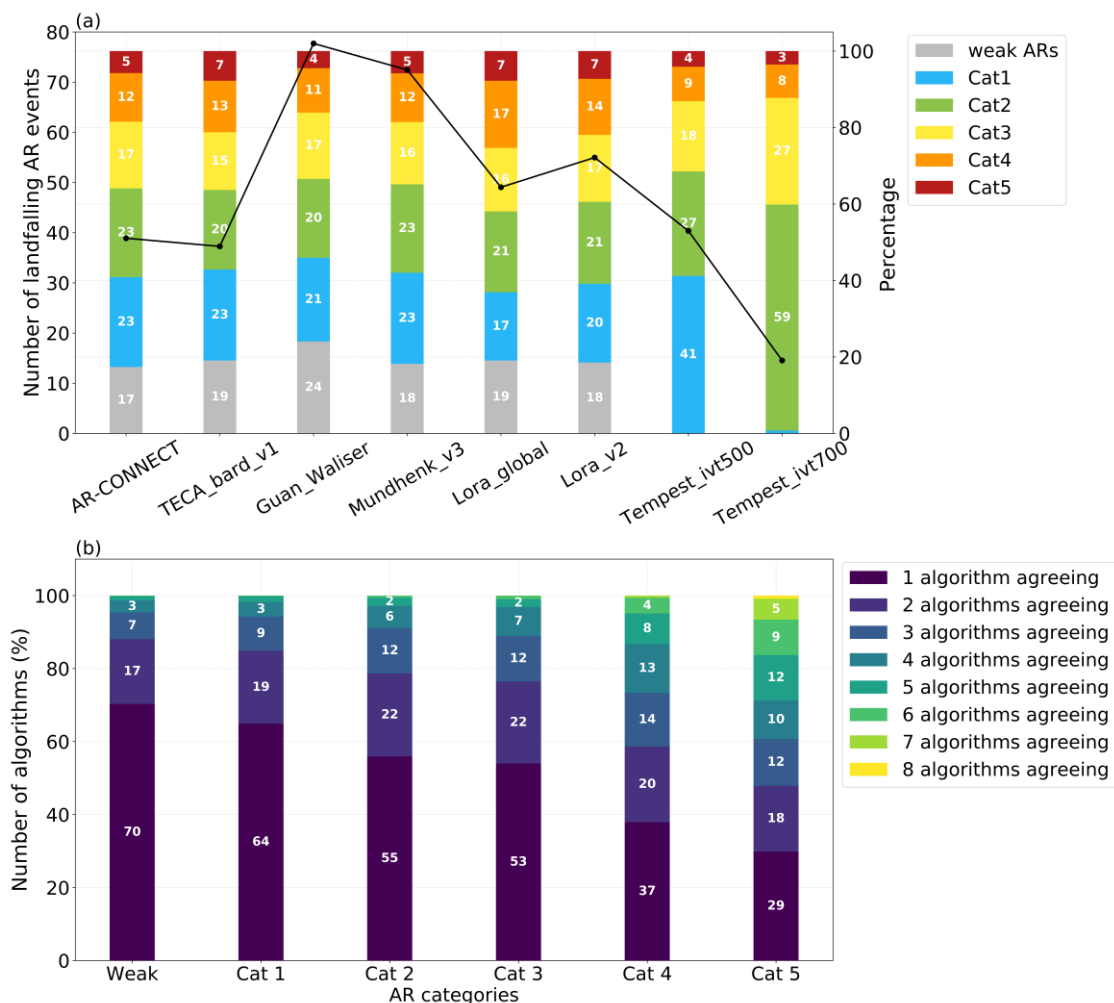
299 Although uncertainties in landfalling ARs have been extensively discussed within the  
300 ARTMIP literature, here we investigate the agreement of algorithms in the life cycle of landfalling  
301 ARs. We focus on the landfalling ARs over the west coast of North America (30°N-60°N) from  
302 November to March, which is the most active season of landfalling activity detected by the  
303 algorithms (not shown). We categorize the landfalling AR events into five categories following  
304 Ralph et al. (2019). The AR scaling criteria account for both landfalling duration and maximum  
305 landfall |IVT|. The AR category 1-5 is defined by maximum |IVT| of 250-1250 kg m<sup>-1</sup> s<sup>-1</sup> and by  
306 |IVT| exceeding 250 kg m<sup>-1</sup> s<sup>-1</sup> for 24-72 hours. Ralph et al. (2019) additionally recognizes  
307 landfalling ARs with |IVT| between 250-500 kg m<sup>-1</sup> s<sup>-1</sup> and duration less than 24 hours as weak  
308 ARs. From a water resources perspective, the weak ARs and Category 1-3 ARs (maximum |IVT|  
309 between 250-1000 kg m<sup>-1</sup> s<sup>-1</sup>) are generally beneficial and Category 4-5 ARs (maximum |IVT|  
310 between 1000-1250 kg m<sup>-1</sup> s<sup>-1</sup>) are mostly harmful primarily due to the risk of flooding and  
311 landslides. In Ralph et al. (2019), the determination of AR category is gridpoint-based, so the  
312 category for the same landfalling AR may vary depending on the location. Here, one AR event is  
313 categorized into one category with the maximum |IVT| over gridpoints and the landfall duration

314 of the entire event. Therefore, this study may overestimate the AR categories comparing to Ralph  
 315 et al. (2019).

316 With the exception of the Tempest family, which misses the weaker categories due to more  
 317 restrictive parameter selections, the number of landfalling AR events ranges from 37 to 78 events  
 318 per season among algorithms (Figure 5a), with the highest number in Guan\_Waliser, which  
 319 captures the most in-land AR activity (Figure 2c). Interestingly, although there is a large  
 320 discrepancy in landfalling event numbers, percentages in each AR category are similarly  
 321 distributed among algorithms. Weak and Category 1-2 ARs take up about 20% of total landfalling  
 322 events respectively for most algorithms. About 15-17% of landfalling ARs are Category 3 and the  
 323 percentage drops to 12-14% for Category 4. About 4-7% of landfalling ARs are attributed to  
 324 Category 5. No weak ARs (weak & Category 1 ARs) are identified with Tempest\_ivt500  
 325 (Tempest\_ivt700). Percentages of Category 4 and 5 ARs are lower in Tempest algorithms, which  
 326 may be due to a shortened landfall duration caused by relatively higher IVT thresholds than other  
 327 algorithms.

328 How does the agreement in algorithms change in different AR categories? For each AR  
 329 category and each algorithm, we create a time series with landfalling stamps: a day is marked as 1  
 330 if it is a landfalling day and 0 otherwise. Next, for each AR category, we add the time series of all  
 331 algorithms to calculate the number of algorithms agreeing on the same landfalling days. For  
 332 example, if the number equals 5, it means five algorithms detect a landfalling AR on that day. Note  
 333 that the number of algorithms in agreement can change during the same landfalling AR event  
 334 because the landfall duration may vary by algorithms. The percentage in Figure 5b is calculated as  
 335 the number of algorithms in agreement divided by the total number of landfalling days in each  
 336 category. The number of algorithms in agreement increases with AR category. 70% of landfalling

337 days by weak ARs are only detected by one algorithm, indicating that most algorithms are not  
 338 detecting the same weak ARs. On the other hand, about 50% of landfalling days affected by  
 339 Category 5 ARs are detected by at least three algorithms. Although the inclusion of the two  
 340 Tempest algorithms may potentially underestimate the number percentage, the result suggests that  
 341 the uncertainty among algorithms is much smaller with stronger ARs.



342  
 343 Figure 5. (a) (Line, left y-axis) Number of landfalling AR events per winter season over the west  
 344 coast of North America. (Bar, right y-axis) Percentage of landfalling events in each AR category.  
 345 (b) Percentage of the number of algorithms in agreement. Numbers in (a-b) annotate the percentage.

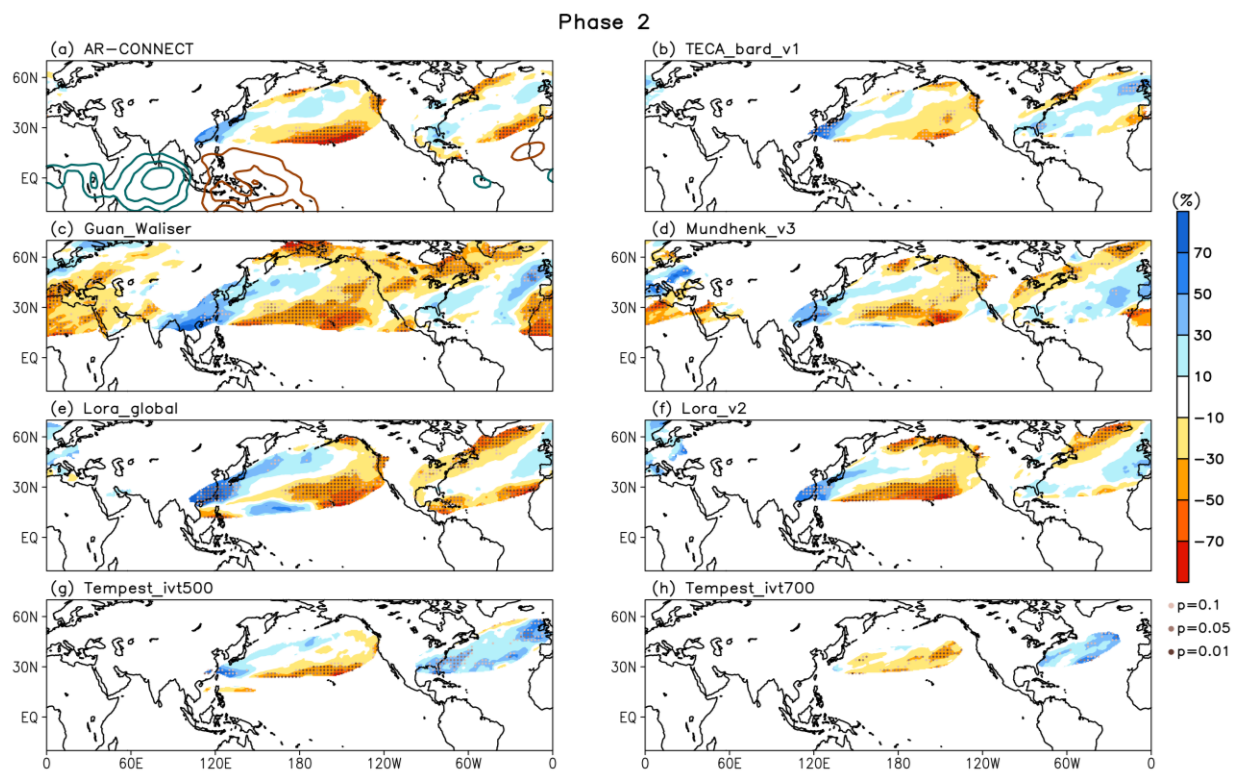
346

#### 347 **4. MJO-AR connections**

348 Previous studies have discussed how ARs may be impacted by the MJO, including  
349 associated landfalling activity, AR-related hydrological impacts, and subseasonal AR prediction  
350 (Baggett et al., 2017; Guan et al., 2013; Guan & Waliser, 2015; Guan et al., 2012; Mundhenk et  
351 al., 2016; Mundhenk et al., 2018; Payne & Magnusdottir, 2014; Ralph et al., 2011). Here, we  
352 examine the linkage between ARs and the MJO from the lifecycle perspective to evaluate the  
353 robustness of such linkages. To investigate the MJO's influence on AR life cycles, we select AR  
354 events that *originate concurrently* with the MJO phases. In each MJO phase, the composite for  
355 each algorithm is calculated by subtracting the respective winter climatology (Supplemental Figure  
356 S5) and dividing by the number of MJO days in that phase. For a clear comparison, all composites  
357 are normalized to show the relative percentage changes.

358 Figure 6 shows the percentage changes in AR lifecycle frequency during MJO phase 2,  
359 when enhanced (suppressed) convection is located over the Indian Ocean (western Pacific). For  
360 each AR event, the lifecycle frequency is calculated as the summation of binary mask for each AR  
361 object within the event and therefore summarizes the overall area impacted by an AR life cycle.  
362 During MJO phase 2, a geopotential high anomaly persists over the North Pacific (Supplemental  
363 Figure 1b) and induces an anticyclonic flow with equatorward and westward flow over the  
364 northeastern Pacific and poleward and eastward flow over the northwestern Pacific (Stan et al.,  
365 2017). Algorithms overall present similar changes in lifecycle frequency during MJO phase 2, with  
366 about 10-30% decrease over the subtropical and northeastern Pacific, and approximately 30-50%  
367 increase near eastern Asia. Most algorithms suggest reduced AR activity over North America,  
368 where Guan\_Waliser shows the strongest reduction, with a nearly 10-30% decrease of in-land  
369 lifecycle frequency between 30°N-60°N. Over the North Atlantic, an approximately 10% increase

370 of lifecycle frequency occurs between 25°N-60°N, which may be associated with the increased  
 371 tropical cyclone activity during MJO phase 2 (Barnston et al., 2015; Maloney & Hartmann, 2000;  
 372 Mo, 2000). The increased lifecycle frequency over the North Atlantic is stronger in  
 373 Tempest\_ivt500 and Tempest\_ivt700, which implies that responses in North Atlantic ARs to the  
 374 MJO may be stronger for ARs with greater intensity.



375  
 376 Figure 6. Shading: percentage changes in cool-season AR lifecycle frequency during MJO phase  
 377 2. Dots mark areas of different p-values. Contour in (a): 20-100-day-filtered OLR anomaly  
 378 (blue/orange means negative/positive value,  $5 \text{ W m}^{-2}$  interval, zero line is omitted).

379  
 380 Algorithms show qualitatively similar changes in AR origin frequency over the North  
 381 Pacific during the MJO phases 1-8 (Figure 7). The origin frequency is meridionally averaged  
 382 between 20°N-40°N which is the latitudinal range of maximum origin frequency (Figure 2). All

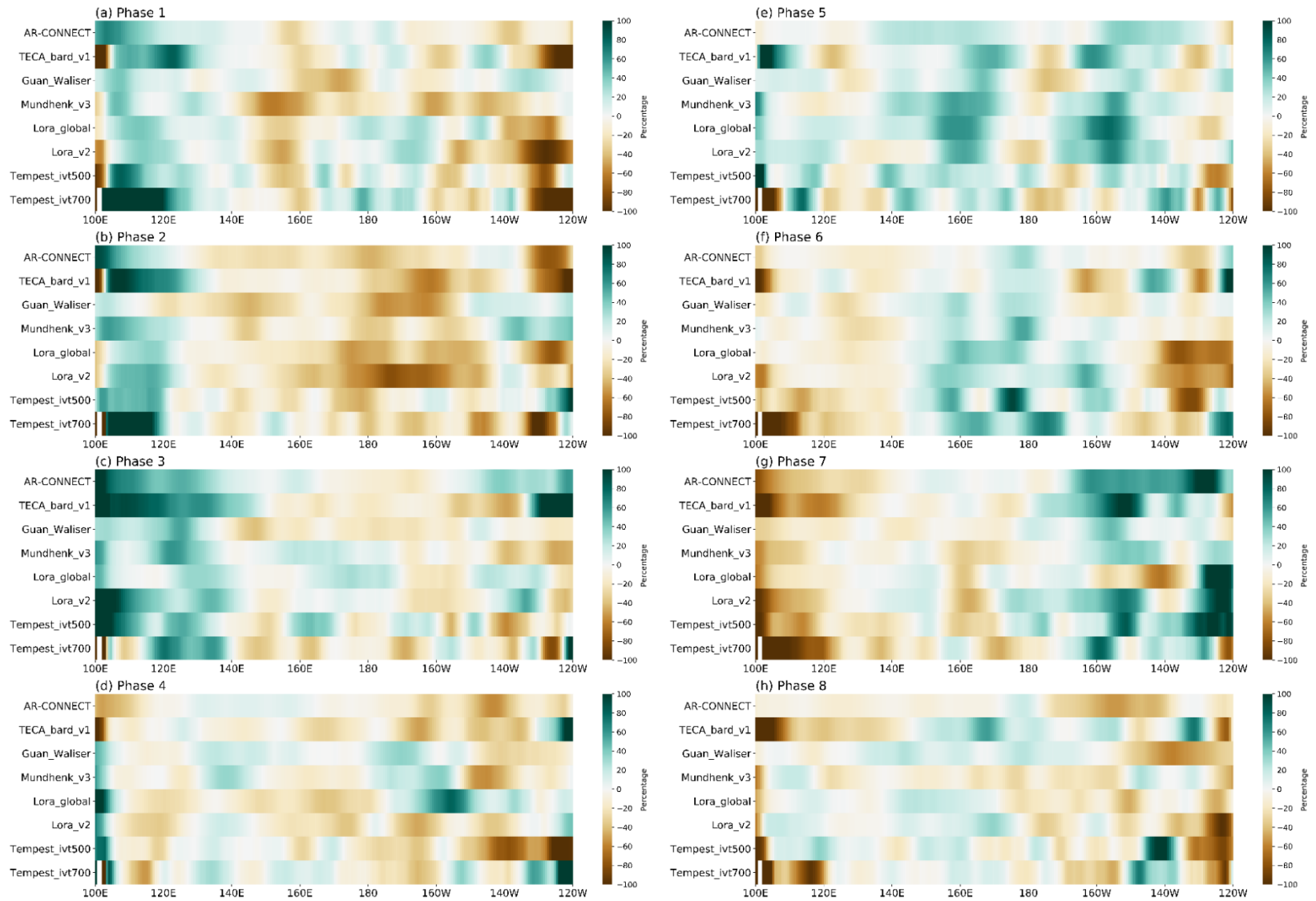
383 algorithms capture the increased origin frequency between 100°E-120°E during phases 1-2 when  
384 the MJO convection is over the Indian Ocean, with an average increase of 35%, excluding the  
385 Tempest\_ivt700 which shows an increase of 200%. The large increase in Tempest\_ivt700 may be  
386 due to its weakest winter climatology among algorithms (Supplemental Figure S5h). The increased  
387 origin frequency extends eastward to 140° E as the MJO convection propagates eastward to the  
388 west lateral of the Maritime Continent during phase 3. The increased origin frequency may be  
389 related to increased moisture content coupled with enhanced tropical convection (Bretherton et al.,  
390 2004; Holloway & Neelin, 2009). Meanwhile, decreased origin frequency emerges near 140°E-  
391 160°E during phases 1-3. Changes in origin frequency over the northwestern Pacific are associated  
392 with a Gill type response to MJO forcing (Bao & Hartmann, 2014; Gill, 1980). Additionally,  
393 decreased origin frequency occurs near 140°W during phase 2, which is associated with the  
394 anomalous high over the northeastern Pacific (Supplemental Figure 1b). On average, the origin  
395 frequency over the northeastern Pacific (170°E-140°W) is decreased by 30%.

396       Roughly opposite changes in origin frequency emerge during MJO phase 5-6 when the  
397 enhanced convection is over the western Pacific (Figure 7e-g). Decreased origin frequency occurs  
398 over eastern Asia and the northwestern Pacific and increased origin frequency emerges between  
399 140°E-160°E. The maximum increase in origin frequency is over the northeastern Pacific, which  
400 is impacted by the anomalous low anomaly during MJO phase 7 (Stan et al., 2017; Supplemental  
401 Figure S1g). This is consistent with previous studies suggesting that AR activity is likely to  
402 increase when enhanced tropical convection is over the western Pacific (phase 6-7) (Guan et al.,  
403 2012; Payne & Magnusdottir, 2014; Spry et al., 2014). Changes during phases 4 and 8 are relatively  
404 weaker and noisier comparing to other MJO phases. The same calculation is done with North  
405 Atlantic AR life cycles (Supplemental Figure S6). Similar changes among algorithms appear



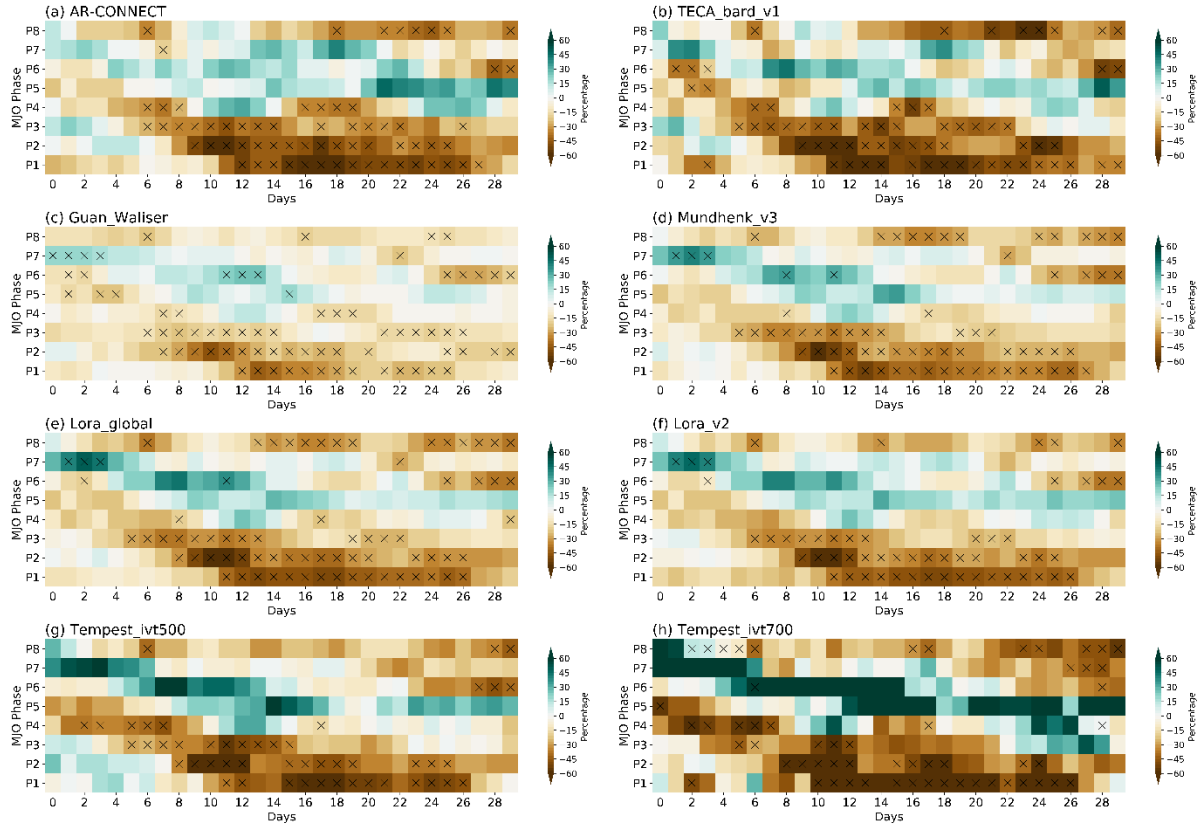
406 during MJO phases 1-2 with increased origin frequency over the northeastern Atlantic which is  
407 consistent with Figure 6. Overall, for both the North Pacific and North Atlantic, changes in AR  
408 origin and lifecycle frequency by the MJO are qualitatively agreeable among detection algorithms,  
409 although regional disagreement exists due to uncertainties in identifying the origin of AR events  
410 and determining object sizes.

411 To evaluate the robustness of the MJO's impact on landfalling ARs, we calculate the  
412 domain average of landfalling AR frequency along the west coast of North America. A mask with  
413 10° longitudinal width is created following the coastline. Three domains are selected including  
414 California, Oregon and Washington, and British Colombia. Figure 8 shows the lagged composites  
415 of percentage changes in landfalling AR frequency over California by MJO phases. For example,  
416 day 0 is when the MJO is in-phase and day 6 represents six days after day 0. The MJO's impact  
417 on landfalling ARs is persistent during the MJO's lifecycle. AR activity over California is  
418 significantly decreased (about 30-45%) from lag 12-24 days after phase 1 to lag 5-14 days after  
419 phase 3 in all algorithms. From lag 13-18 days after phase 5 to lag 0-5 days after phase 7, an  
420 approximate increase of 25-35% in AR frequency emerges. A similar pattern is shown in  
421 Mundhenk et al. (2018). Responses in *Tempest\_ivt700* are particularly intense, with an  
422 approximate 70% decrease during phases 1-3 and a nearly 80% increase during phases 5-7. This  
423 could be because *Tempest\_ivt700* has a relatively weaker climatology because of the higher IVT  
424 threshold (Supplemental Figure S5h); alternatively, stronger ARs may be more sensitive to the  
425 MJO. Similar but shifted patterns appear in the lagged composites of Oregon and Washington as  
426 well as British Colombia (Supplemental Figure S7-8).



427

428 Figure 7. Percentage changes in North Pacific origin frequency during (a-h) MJO phase 1-8.



429

430 Figure 8. Percentage changes in landfalling AR frequency over California during MJO phase 1-8.

431 The x-axis represents the days after an in-phase MJO. The dot marks the day that exceeds the 95%

432 significant level of a one-sample t-test.

433

434 **5. ENSO-AR connections**

435 How ENSO modulates AR activity has been examined in several studies (e.g., Guan &

436 Waliser, 2015; Kim et al., 2017; Mundhenk et al., 2016; Patricola et al., 2020; Payne &

437 Magnusdottir, 2014; Ryoo et al., 2013), especially over the northeastern Pacific. During El Niño

438 winters when the anomalously warm SST gathers over the tropical eastern Pacific (Figure 9a), a

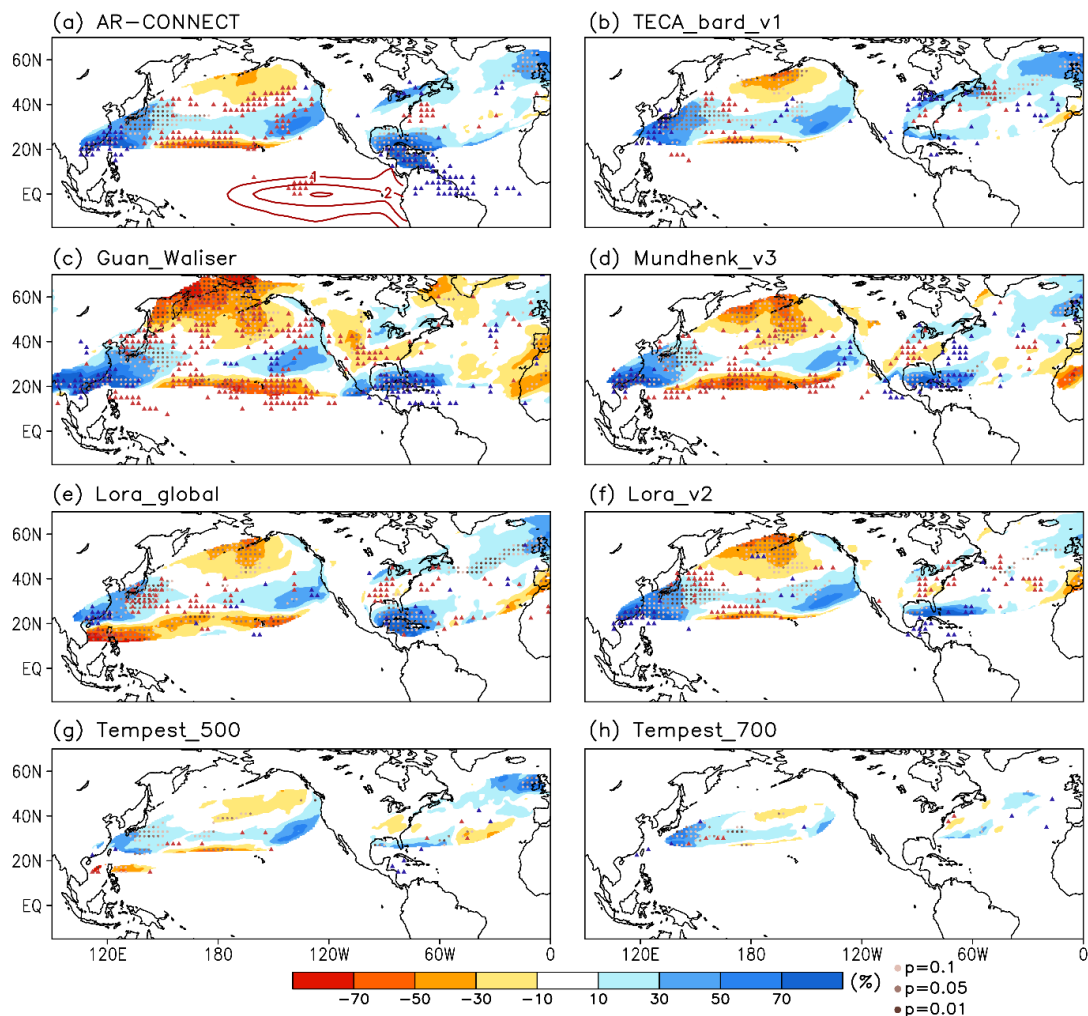
439 deepened Aleutian Low prevails over the northeastern Pacific, which is associated with the

440 equatorward-shifted and eastward-extended subtropical jet (not shown). Previous studies have

441 concluded that correspondingly, more zonal moisture transport occurs during El Niño winter,

442 which is represented by increased AR activity over the northeastern Pacific and the west coast of  
443 U.S. around 30°N-45°N (e.g., Kim et al., 2017; McGuirk et al., 1987; Patricola et al., 2020).

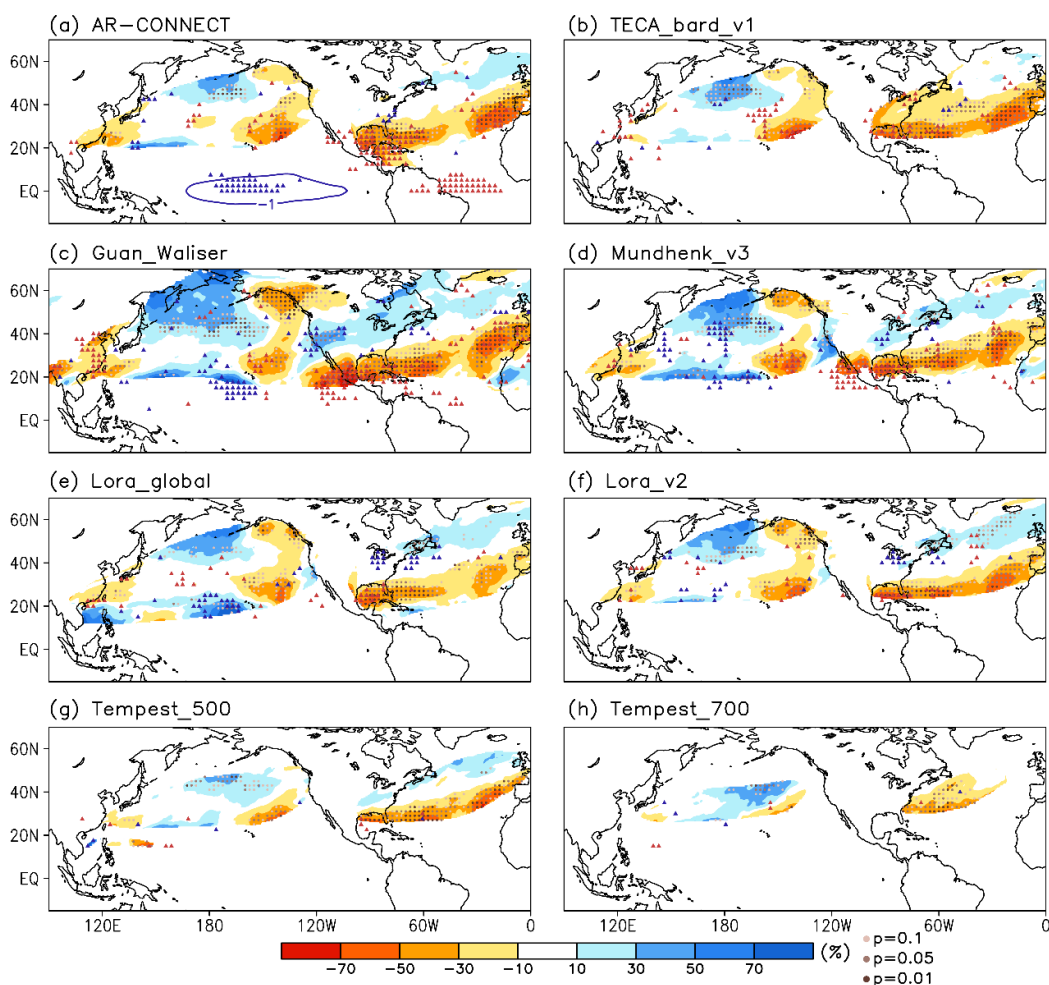
444 Here, we calculate the changes in lifecycle frequency to evaluate the robustness of the  
445 ENSO-AR connection. All algorithms show a zonal band of increased lifecycle frequency between  
446 20°N-40°N with two maximum centers over the northeastern and northwestern Pacific. Changes  
447 in AR activity over the northeastern Pacific are closely modulated by the deepened Aleutian Low  
448 (Kim et al., 2017). All algorithms demonstrate a 10-30% increase of lifecycle frequency between  
449 30°N-45°N which is associated with the northeastward IVT anomaly at the south branch of the  
450 intensified Aleutian Low (e.g. Figure 2a in Kim et al. (2017)). The maximum decrease in lifecycle  
451 frequency between 40°N-60°N is associated with the southwestward IVT anomaly at the north  
452 branch of the anomalous low. Over the northwestern Pacific, the AR origin frequency is  
453 significantly increased by at least 30% over eastern Asia. The decreased origin frequency near  
454 20°N is linked to the decreased lifecycle frequency over the subtropical central Pacific.  
455 Mechanisms associated with the changes in AR origin frequency over the northwestern Pacific  
456 have not been discussed extensively by previous studies. Possible hypotheses include impacts from  
457 the subtropical jet and geopotential height pattern (Patricola et al., 2020), or the joint impact from  
458 the MJO and ENSO (Lau & Chan, 1988; Moon et al., 2011), which we will investigate in the future  
459 study. Significant changes also appear over the North Atlantic: all algorithms show the increased  
460 origin and lifecycle frequency along the U.S. east coast, which is likely associated with the  
461 increased extratropical cyclone activity during El Niño (Chang et al., 2002; Eichler & Higgins,  
462 2006; Hirsch et al., 2001).



463  
 464 Figure 9. Shading: percentage changes in AR lifecycle frequency during El Niño years. Dots mark  
 465 the areas of different p-values. Blue/red solid triangle markers indicate areas with  
 466 increased/decreased origin frequency exceeding 30% and passing the 95% confidence level of a  
 467 one-sample t-test. Contours in (a) indicate the SST anomaly during El Niño.

468  
 469 A nearly opposite pattern of changes in lifecycle frequency is shown during La Niña  
 470 winters when cold SST anomaly concentrates in the central and eastern Pacific (Figure 10a).  
 471 Changes in lifecycle frequency present consistent patterns over the northeastern Pacific in all  
 472 algorithms. Decreased frequency, with a peak of 70%, appears near the U.S. west coast. Increased

473 lifecycle frequency occurs between 40°N-60°N over the central Pacific, which is associated with  
 474 the northeastward IVT anomaly at the northwest branch of the anomalous high. Opposite responses  
 475 in AR origins and lifecycle frequency emerge over the northwestern Pacific but in a weaker  
 476 amplitude comparing to El Niño. The asymmetry between El Niño and La Niña is discussed in  
 477 previous studies (e.g., An et al., 2005; An & Jin, 2004; Gershunov & Barnett, 1998; Hoerling et  
 478 al., 1997). Interestingly, a regional increase in lifecycle frequency occurs over the western US  
 479 coast near 30°N during La Niña in some algorithms (Figure 10c-f), which tends to be similar during  
 480 El Niño. Also, a roughly 50% decrease in lifecycle frequency is shown over the North Atlantic  
 481 between 20°N-40°N and extends eastward to the southern part of the west coast of Europe.



482

483 Figure 10. Same as Figure 9 but for La Niña years.

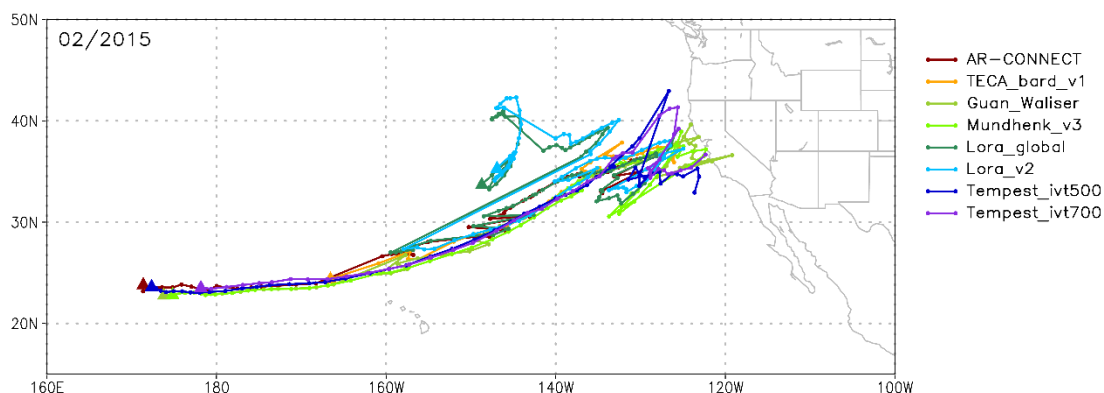
484

485 **6. Summary and discussion**

486         It has been a community effort to understand and quantify the uncertainties in AR research  
487 caused by detection algorithms. In this study, we specifically investigate the uncertainties of AR  
488 life cycles stemming from detection algorithms including their characteristics and connections to  
489 climate variabilities. Eight global algorithms are selected from the ARTMIP Tier 1 dataset. Results  
490 suggest that uncertainties in lifecycle characteristics (such as number of events, lifetime, travel  
491 distance, propagation speed, and intensity) can be large among algorithms. Such uncertainties are  
492 mainly caused by discrepancies in object sizes and spatiotemporal connectivity due to different  
493 algorithm design (e.g., choice of threshold and geometric constraint). Previous literature discussed  
494 the sensitivity of AR characteristics to detection methods concerning algorithm development (e.g.,  
495 Guan & Waliser, 2015; Mundhenk et al., 2016; Rutz et al., 2014), our study extends this discussion  
496 to multiple algorithms with the perspective of AR life cycles.

497         Because of the significant hydrological impacts of ARs, the spread in landfalling AR  
498 activity over the west coast of North America by detection algorithms has been extensively  
499 discussed by previous ARTMIP publications (references in Section 1). We evaluate the spread in  
500 number of landfalling AR events and the agreement on landfalling AR category impact scaling  
501 among algorithms. The number of landfalling AR life cycles can vary from 15 events per winter  
502 to 78 events per winter by different algorithms. Results suggest that algorithms' agreement in AR  
503 landfalling days increases with higher AR categories although the lifecycle characteristics may  
504 vary. For example, Figure 11 shows the propagation tracks identified by different algorithms of a  
505 Category 5 AR that made landfall over California around February 7, 2015, which is in association  
506 with hourly precipitation amounts  $> 8$  mm/hr (Cordeira et al., 2017). All eight algorithms detected

507 this landfalling AR. However, while most algorithms identify the origin of this AR event between  
 508 25°N, 170°E-160°W and show the northeastward propagation of moisture transport, two  
 509 algorithms suggest different origin locations near 35°N, 150°W, which is likely due to merging of  
 510 objects during propagation. The propagation tracks start to wobble when approaching to the coast  
 511 because the shape and size of AR objects may change quickly as rapid depletion of IVT via  
 512 precipitation upon landfall. Figure 11 indicates that when focusing on the physical processes such  
 513 as mechanisms for AR origins and the path along which the AR propagates, the uncertainty  
 514 introduced by detection algorithms may impede the understanding and interpretation of AR  
 515 activity. For the same moisture transport event, the points of origin and termination vary by  
 516 algorithms. This could be problematic when predicting the evolution of ARs or forecasting AR-  
 517 related precipitations.



518  
 519 Figure 11. Example of propagation tracks of a landfalling AR event in early February 2015. Solid  
 520 triangles mark the locations of AR origins detected by algorithms.

521  
 522 Additionally, the robustness of the MJO-AR and ENSO-AR connections across different  
 523 algorithms is discussed. The overall AR responses to the MJO and ENSO are maintained despite  
 524 differences in detection algorithms, indicating that the uncertainties in AR life cycles by detection  
 525 algorithms may be smoothed out when investigating AR activity in a time scale longer than ARs



526 (such as connections with the MJO and ENSO). However, disagreements in regional distribution  
527 of origin and total frequency imply the challenges in quantifying AR's response to climate  
528 variabilities.

529         Although there is a lack of consensus for a quantitative definition of ARs, various studies  
530 have quantitatively defined ARs for analysis and modeling, which primarily leads to uncertainties  
531 in AR measures (Rutz et al., 2019; Shields et al., 2018) including the spread in AR life cycles  
532 discussed in this study. Such uncertainties could also cause variations in quantifying changes of  
533 future ARs such as object sizes, frequency, and other lifecycle characteristics (Espinoza et al.,  
534 2018; Radic et al., 2015; Shields & Kiehl, 2016a). A better understanding of the physical processes  
535 associated with different stages in AR life cycle (such as origin, propagation, landfall, and  
536 termination) is crucial to mitigate uncertainties in AR-related research. This study provides a  
537 useful tool to analyze the mechanisms associated with each stage of AR life cycles and to conduct  
538 uncertainty analysis with multiple algorithms. An effort like this could help to pave the way toward  
539 a quantitative theory of AR origins and terminations, which has great implications on improving  
540 AR predictions and advancing the understanding of future ARs.

541

542

543  
544  
545  
546  
547  
548  
549  
550  
551  
552  
553  
554  
555  
556  
557  
558  
559

### Acknowledgments

This study was funded by the Director, Office of Science, Office of Biological and Environmental Research of the U.S. Department of Energy Regional and Global Climate Modeling Program (RGCM) “the Calibrated and Systematic Characterization, Attribution and Detection of Extremes (CASCADE)” Science Focus Area (award no. DE-AC02-05CH11231). Analysis was performed using the National Energy Research Scientific Computing Center (NERSC).

All ARTMIP data are available from the Climate Data Gateway, DOI:10.5065/D6R78D1M (ARTMIP Tier 1 Catalogues)

The OLR is provided by the NOAA/OAR/ESRL PSD, Boulder, Colorado, USA, from their Web site at [https://psl.noaa.gov/data/gridded/data.interp\\_OLR.html](https://psl.noaa.gov/data/gridded/data.interp_OLR.html).

The Extended Reconstructed SST v5 data is provided by the NOAA/OAR/ESRL PSL, Boulder, Colorado, USA, from their Web site at <https://psl.noaa.gov/data/gridded/data.noaa.ersst.v5.html>.

The Real-time Multivariate MJO index is obtained from the Bureau of Meteorology from Australian Government at <http://www.bom.gov.au/climate/mjo/graphics/rmm.74toRealtime.txt>.

560 **Reference**

- 561 An, S. I., Ham, Y. G., Kug, J. S., Jin, F. F., & Kang, I. S. (2005). El Niño–La Niña Asymmetry in  
562 the Coupled Model Intercomparison Project Simulations\*. *Journal of Climate*, *18*(14),  
563 2617-2627. doi:10.1175/jcli3433.1
- 564 An, S. I., & Jin, F. F. (2004). Nonlinearity and Asymmetry of ENSO. *Journal of Climate*, *17*(12),  
565 2399-2412. doi:10.1175/1520-0442(2004)017<2399:NAAOE>2.0.CO;2
- 566 Baggett, C. F., Barnes, E. A., Maloney, E. D., & Mundhenk, B. D. (2017). Advancing atmospheric  
567 river forecasts into subseasonal-to-seasonal time scales. *Geophysical Research Letters*,  
568 *44*(14), 7528-7536. doi:10.1002/2017gl074434
- 569 Bao, M., & Hartmann, D. L. (2014). The response to MJO-like forcing in a nonlinear shallow-  
570 water model. *Geophysical Research Letters*, *41*(4), 1322-1328. doi:10.1002/2013gl057683
- 571 Barnston, A. G., Vigaud, N., Long, L. N., Tippett, M. K., & Schemm, J. E. (2015). Atlantic  
572 Tropical Cyclone Activity in Response to the MJO in NOAA’s CFS Model. *Monthly*  
573 *Weather Review*, *143*(12), 4905-4927. doi:10.1175/mwr-d-15-0127.1
- 574 Bretherton, C. S., Peters, M. E., & Back, L. E. (2004). Relationships between water vapor path  
575 and precipitation over the tropical oceans. *Journal of Climate*, *17*(7), 1517-1528. doi:Doi  
576 10.1175/1520-0442(2004)017<1517:Rbwvpa>2.0.Co;2
- 577 Chang, E. K. M., Lee, S. Y., & Swanson, K. L. (2002). Storm track dynamics. *Journal of Climate*,  
578 *15*(16), 2163-2183. doi:Doi 10.1175/1520-0442(2002)015<02163:Std>2.0.Co;2
- 579 Chen, X. D., Leung, L. R., Wigmosta, M., & Richmond, M. (2019). Impact of Atmospheric Rivers  
580 on Surface Hydrological Processes in Western U.S. Watersheds. *Journal of Geophysical*  
581 *Research: Atmospheres*, *124*(16), 8896-8916. doi:10.1029/2019jd030468

- 582 Cordeira, J. M., Ralph, F. M., Martin, A., Gaggini, N., Spackman, J. R., Neiman, P. J., . . . Pierce,  
583 R. (2017). Forecasting Atmospheric Rivers during CalWater 2015. *Bulletin of the*  
584 *American Meteorological Society*, 98(3), 449-459. doi:10.1175/bams-d-15-00245.1
- 585 DeFlorio, M. J., Waliser, D. E., Guan, B., Lavers, D. A., Ralph, F. M., & Vitart, F. (2018). Global  
586 Assessment of Atmospheric River Prediction Skill. *Journal of Hydrometeorology*, 19(2),  
587 409-426. doi:10.1175/Jhm-D-17-0135.1
- 588 DeFlorio, M. J., Waliser, D. E., Guan, B., Ralph, F. M., & Vitart, F. (2018). Global evaluation of  
589 atmospheric river subseasonal prediction skill. *Climate Dynamics*, 52(5-6), 3039-3060.  
590 doi:10.1007/s00382-018-4309-x
- 591 Dettinger, M. D. (2013). Atmospheric Rivers as Drought Busters on the US West Coast. *Journal*  
592 *of Hydrometeorology*, 14(6), 1721-1732. doi:10.1175/Jhm-D-13-02.1
- 593 Dettinger, M. D., Ralph, F. M., Das, T., Neiman, P. J., & Cayan, D. R. (2011). Atmospheric Rivers,  
594 Floods and the Water Resources of California. *Water*, 3(2), 445-478.  
595 doi:10.3390/w3020445
- 596 Eichler, T., & Higgins, W. (2006). Climatology and ENSO-Related Variability of North American  
597 Extratropical Cyclone Activity. *Journal of Climate*, 19(10), 2076-2093.  
598 doi:10.1175/JCLI3725.1
- 599 Espinoza, V., Waliser, D. E., Guan, B., Lavers, D. A., & Ralph, F. M. (2018). Global Analysis of  
600 Climate Change Projection Effects on Atmospheric Rivers. *Geophysical Research Letters*,  
601 45(9), 4299-4308. doi:10.1029/2017gl076968
- 602 Gelaro, R., McCarty, W., Suarez, M. J., Todling, R., Molod, A., Takacs, L., . . . Zhao, B. (2017).  
603 The Modern-Era Retrospective Analysis for Research and Applications, Version 2  
604 (MERRA-2). *J Clim*, Volume 30(Iss 13), 5419-5454. doi:10.1175/JCLI-D-16-0758.1

- 605 Gershunov, A., & Barnett, T. P. (1998). ENSO Influence on Intraseasonal Extreme Rainfall and  
606 Temperature Frequencies in the Contiguous United States: Observations and Model  
607 Results. *Journal of Climate*, *11*(7), 1575-1586. doi:10.1175/1520-  
608 0442(1998)011<1575:Eioier>2.0.Co;2
- 609 Gershunov, A., Shulgina, T., Ralph, F. M., Lavers, D. A., & Rutz, J. J. (2017). Assessing the  
610 climate-scale variability of atmospheric rivers affecting western North America.  
611 *Geophysical Research Letters*, *44*(15), 7900-7908. doi:10.1002/2017gl074175
- 612 Gill, A. E. (1980). Some simple solutions for heat-induced tropical circulation. *Quarterly Journal*  
613 *of the Royal Meteorological Society*, *106*(449), 447-462. doi:10.1002/qj.49710644905
- 614 Gorodetskaya, I. V., Tsukernik, M., Claes, K., Ralph, M. F., Neff, W. D., & Van Lipzig, N. P. M.  
615 (2014). The role of atmospheric rivers in anomalous snow accumulation in East Antarctica.  
616 *Geophysical Research Letters*, *41*(17), 6199-6206. doi:10.1002/2014gl060881
- 617 Guan, B., Molotch, N. P., Waliser, D. E., Fetzer, E. J., & Neiman, P. J. (2013). The 2010/2011  
618 snow season in California's Sierra Nevada: Role of atmospheric rivers and modes of large-  
619 scale variability. *Water Resources Research*, *49*(10), 6731-6743. doi:10.1002/wrcr.20537
- 620 Guan, B., & Waliser, D. E. (2015). Detection of atmospheric rivers: Evaluation and application of  
621 an algorithm for global studies. *Journal of Geophysical Research-Atmospheres*, *120*(24),  
622 12514-12535. doi:10.1002/2015jd024257
- 623 Guan, B., Waliser, D. E., Molotch, N. P., Fetzer, E. J., & Neiman, P. J. (2012). Does the Madden–  
624 Julian Oscillation Influence Wintertime Atmospheric Rivers and Snowpack in the Sierra  
625 Nevada? *Monthly Weather Review*, *140*(2), 325-342. doi:10.1175/mwr-d-11-00087.1

- 626 Halpern, D., & Woiceshyn, P. M. (1999). Onset of the Somali Jet in the Arabian Sea during June  
627 1997. *Journal of Geophysical Research: Oceans*, *104*(C8), 18041-18046.  
628 doi:10.1029/1999jc900141
- 629 Hirsch, M. E., DeGaetano, A. T., & Colucci, S. J. (2001). An East Coast Winter Storm Climatology.  
630 *Journal of Climate*, *14*(5), 882-899. doi:10.1175/1520-  
631 0442(2001)014<0882:Aecwsc>2.0.Co;2
- 632 Hoerling, M. P., Kumar, A., & Zhong, M. (1997). El Niño, La Niña, and the Nonlinearity of Their  
633 Teleconnections. *Journal of Climate*, *10*(8), 1769-1786. doi:10.1175/1520-  
634 0442(1997)010<1769:Enolna>2.0.Co;2
- 635 Holloway, C. E., & Neelin, J. D. (2009). Moisture Vertical Structure, Column Water Vapor, and  
636 Tropical Deep Convection. *Journal of the Atmospheric Sciences*, *66*(6), 1665-1683.  
637 doi:10.1175/2008jas2806.1
- 638 Hu, H., Dominguez, F., Wang, Z., Lavers, D. A., Zhang, G., & Ralph, F. M. (2017). Linking  
639 Atmospheric River Hydrological Impacts on the U.S. West Coast to Rossby Wave  
640 Breaking. *Journal of Climate*, *30*(9), 3381-3399. doi:10.1175/jcli-d-16-0386.1
- 641 Huang, B., Thorne, P. W., Banzon, V. F., Boyer, T., Chepurin, G., Lawrimore, J. H., . . . Zhang,  
642 H. (2017). Extended Reconstructed Sea Surface Temperature, Version 5 (ERSSTv5):  
643 Upgrades, Validations, and Intercomparisons. *Journal of Climate*, *30*(20), 8179-8205.  
644 doi:10.1175/jcli-d-16-0836.1
- 645 Huning, L. S., Margulis, S. A., Guan, B., Waliser, D. E., & Neiman, P. J. (2017). Implications of  
646 Detection Methods on Characterizing Atmospheric River Contribution to Seasonal  
647 Snowfall Across Sierra Nevada, USA. *Geophysical Research Letters*, *44*(20), 10,445-  
648 410,453. doi:10.1002/2017gl075201

- 649 Kim, H., Zhou, Y., & Alexander, M. A. (2017). Changes in atmospheric rivers and moisture  
650 transport over the Northeast Pacific and western North America in response to ENSO  
651 diversity. *Climate Dynamics*, 1-14. doi:10.1007/s00382-017-3598-9
- 652 Lau, K. M., & Chan, P. H. (1988). Intraseasonal and Interannual Variations of Tropical Convection:  
653 A Possible Link between the 40–50 Day Oscillation and ENSO? *Journal of the*  
654 *Atmospheric Sciences*, 45(3), 506-521. doi:10.1175/1520-  
655 0469(1988)045<0506:laivot>2.0.Co;2
- 656 Lavers, D. A., Allan, R. P., Villarini, G., Lloyd-Hughes, B., Brayshaw, D. J., & Wade, A. J. (2013).  
657 Future changes in atmospheric rivers and their implications for winter flooding in Britain.  
658 *Environmental Research Letters*, 8(3). doi:Artn 03401010.1088/1748-9326/8/3/034010
- 659 Lavers, D. A., Allan, R. P., Wood, E. F., Villarini, G., Brayshaw, D. J., & Wade, A. J. (2011).  
660 Winter floods in Britain are connected to atmospheric rivers. *Geophysical Research Letters*,  
661 38(23), L23803. doi:Artn L2380310.1029/2011gl049783
- 662 Lavers, D. A., Pappenberger, F., & Zsoter, E. (2014). Extending medium-range predictability of  
663 extreme hydrological events in Europe. *Nature Communications*, 5, 5382.  
664 doi:10.1038/ncomms6382
- 665 Liebmann, B., & Smith, C. A. (1996). Description of a complete (interpolated) outgoing longwave  
666 radiation dataset. *Bulletin of the American Meteorological Society*, 77(6), 1275-1277.  
667 Retrieved from <Go to ISI>://WOS:A1996VC04300013
- 668 Lora, J. M., Mitchell, J. L., Risi, C., & Tripathi, A. E. (2017). North Pacific atmospheric rivers and  
669 their influence on western North America at the Last Glacial Maximum. *Geophysical*  
670 *Research Letters*, 44(2), 1051-1059. doi:10.1002/2016gl071541

- 671 Maloney, E. D., & Hartmann, D. L. (2000). Modulation of Hurricane Activity in the Gulf of  
672 Mexico by the Madden-Julian Oscillation. *Science*, 287(5460), 2002.  
673 doi:10.1126/science.287.5460.2002
- 674 McClenny, E., Ullrich, P. A., Grotjahn, R. (2020) Sensitivity of atmospheric river vapor transport  
675 and precipitation to uniform sea-surface temperature increases.  
676 <https://doi.org/10.5281/zenodo.3659310>
- 677 McGuirk, J. P., Thompson, A. H., & Smith, N. R. (1987). Moisture Bursts over the Tropical Pacific  
678 Ocean. *Monthly Weather Review*, 115(4), 787-798. doi:10.1175/1520-  
679 0493(1987)115<0787:Mbottp>2.0.Co;2
- 680 Mo, K. C. (2000). The Association between Intraseasonal Oscillations and Tropical Storms in the  
681 Atlantic Basin. *Monthly Weather Review*, 128(12), 4097-4107. doi:10.1175/1520-  
682 0493(2000)129<4097:Tabioa>2.0.Co;2
- 683 Moon, J. Y., Wang, B., & Ha, K. J. (2011). ENSO regulation of MJO teleconnection. *Climate*  
684 *Dynamics*, 37(5-6), 1133-1149. doi:10.1007/s00382-010-0902-3
- 685 Mundhenk, B. D., Barnes, E. A., & Maloney, E. D. (2016). All-Season Climatology and  
686 Variability of Atmospheric River Frequencies over the North Pacific. *Journal of Climate*,  
687 29(13), 4885-4903. doi:10.1175/Jcli-D-15-0655.1
- 688 Mundhenk, B. D., Barnes, E. A., Maloney, E. D., & Baggett, C. F. (2018). Skillful empirical  
689 subseasonal prediction of landfalling atmospheric river activity using the Madden–Julian  
690 oscillation and quasi-biennial oscillation. *npj Climate and Atmospheric Science*, 1(1),  
691 20177. doi:10.1038/s41612-017-0008-2
- 692 Neiman, P. J., Ralph, F. M., Moore, B. J., Hughes, M., Mahoney, K. M., Cordeira, J. M., &  
693 Dettinger, M. D. (2013). The Landfall and Inland Penetration of a Flood-Producing



- 694 Atmospheric River in Arizona. Part I: Observed Synoptic-Scale, Orographic, and  
695 Hydrometeorological Characteristics. *Journal of Hydrometeorology*, 14(2), 460-484.  
696 doi:10.1175/Jhm-D-12-0101.1
- 697 Neiman, P. J., Ralph, F. M., Wick, G. A., Lundquist, J. D., & Dettinger, M. D. (2008).  
698 Meteorological characteristics and overland precipitation impacts of atmospheric rivers  
699 affecting the West Coast of North America based on eight years of SSM/I satellite  
700 observations. *Journal of Hydrometeorology*, 9(1), 22-47. doi:10.1175/2007jhm855.1
- 701 Newell, R. E., Newell, N. E., Zhu, Y., & Scott, C. (1992). Tropospheric Rivers - a Pilot-Study.  
702 *Geophysical Research Letters*, 19(24), 2401-2404. doi:Doi 10.1029/92gl02916
- 703 O'Brien, T. A., Risser, M. D., Loring, B., Elbashandy, A. A., Krishnan, H., Johnson, J., . . . Collins,  
704 W. D. (2020). Detection of Atmospheric Rivers with Inline Uncertainty Quantification:  
705 TECA-BARD v1.0. *Geosci. Model Dev. Discuss.*, 2020, 1-20. doi:10.5194/gmd-2020-55
- 706 Patricola, C. M., O'Brien, J. P., Risser, M. D., Rhoades, A. M., O'Brien, T. A., Ullrich, P. A., . . .  
707 Collins, W. D. (2020). Maximizing ENSO as a source of western US hydroclimate  
708 predictability. *Climate Dynamics*, 54(1-2), 351-372. doi:10.1007/s00382-019-05004-8
- 709 Payne, A. E., & Magnusdottir, G. (2014). Dynamics of Landfalling Atmospheric Rivers over the  
710 North Pacific in 30 Years of MERRA Reanalysis. *Journal of Climate*, 27(18), 7133-7150.  
711 doi:10.1175/Jcli-D-14-00034.1
- 712 Payne, A. E., & Magnusdottir, G. (2015). An evaluation of atmospheric rivers over the North  
713 Pacific in CMIP5 and their response to warming under RCP 8.5. *Journal of Geophysical  
714 Research-Atmospheres*, 120(21), 11173-11190. doi:10.1002/2015jd023586
- 715 Radic, V., Cannon, A. J., Menounos, B., & Gi, N. (2015). Future changes in autumn atmospheric  
716 river events in British Columbia, Canada, as projected by CMIP5 global climate models.

- 717 *Journal of Geophysical Research-Atmospheres*, 120(18), 9279-9302.  
718 doi:10.1002/2015jd023279
- 719 Ralph, F. M., Neiman, P. J., Kiladis, G. N., Weickmann, K., & Reynolds, D. W. (2011). A  
720 Multiscale Observational Case Study of a Pacific Atmospheric River Exhibiting Tropical-  
721 Extratropical Connections and a Mesoscale Frontal Wave. *Monthly Weather Review*,  
722 139(4), 1169-1189. doi:10.1175/2010mwr3596.1
- 723 Ralph, F. M., Neiman, P. J., Wick, G. A., Gutman, S. I., Dettinger, M. D., Cayan, D. R., & White,  
724 A. B. (2006). Flooding on California's Russian River: Role of atmospheric rivers.  
725 *Geophysical Research Letters*, 33(13). doi:Artn L1380110.1029/2006gl026689
- 726 Ralph, F. M., Rutz, J. J., Cordeira, J. M., Dettinger, M., Anderson, M., Reynolds, D., . . .  
727 Smallcomb, C. (2019). A Scale to Characterize the Strength and Impacts of Atmospheric  
728 Rivers. *Bulletin of the American Meteorological Society*, 100(2), 269-290.  
729 doi:10.1175/Bams-D-18-0023.1
- 730 Ralph, F. M., Wilson, A. M., Shulgina, T., Kawzenuk, B., Sellars, S., Rutz, J. J., . . . Wick, G. A.  
731 (2018). ARTMIP-early start comparison of atmospheric river detection tools: how many  
732 atmospheric rivers hit northern California's Russian River watershed? *Climate Dynamics*,  
733 52(7-8), 4973-4994. doi:10.1007/s00382-018-4427-5
- 734 Rhoades, A. M., Jones, A. D., O'Brien, T. A., O'Brien, J. P., Ullrich, P. A., & Zarzycki, C. M.  
735 (2020). Influences of North Pacific Ocean Domain Extent on the Western U.S. Winter  
736 Hydroclimatology in Variable-Resolution CESM. *Journal of Geophysical Research:*  
737 *Atmospheres*, 125(14), e2019JD031977. doi:10.1029/2019jd031977
- 738 Rutz, J. J., Shields, C. A., Lora, J. M., Payne, A. E., Guan, B., Ullrich, P., . . . Viale, M. (2019).  
739 The Atmospheric River Tracking Method Intercomparison Project (ARTMIP):

- 740 Quantifying Uncertainties in Atmospheric River Climatology. *Journal of Geophysical*  
741 *Research: Atmospheres*, 124(24), 13777-13802. doi:10.1029/2019jd030936
- 742 Rutz, J. J., Steenburgh, W. J., & Ralph, F. M. (2014). Climatological Characteristics of  
743 Atmospheric Rivers and Their Inland Penetration over the Western United States. *Monthly*  
744 *Weather Review*, 142(2), 905-921. doi:10.1175/Mwr-D-13-00168.1
- 745 Ryoo, J. M., Kaspi, Y., Waugh, D. W., Kiladis, G. N., Waliser, D. E., Fetzner, E. J., & Kim, J.  
746 (2013). Impact of Rossby Wave Breaking on U.S. West Coast Winter Precipitation during  
747 ENSO Events. *Journal of Climate*, 26(17), 6360-6382. doi:10.1175/Jcli-D-12-00297.1
- 748 Sellars, S. L., Gao, X. G., & Sorooshian, S. (2015). An Object-Oriented Approach to Investigate  
749 Impacts of Climate Oscillations on Precipitation: A Western United States Case Study.  
750 *Journal of Hydrometeorology*, 16(2), 830-842. doi:10.1175/Jhm-D-14-0101.1
- 751 Sellars, S. L., Nguyen, P., Chu, W., Gao, X., Hsu, K. L., & Sorooshian, S. (2013). Computational  
752 Earth Science: Big Data Transformed Into Insight. *Eos, Transactions American*  
753 *Geophysical Union*, 94(32), 277-278. doi:10.1002/2013eo320001
- 754 Shearer, E. J., Nguyen, P., Sellars, S. L., Analui, B., Kawzenuk, B., Hsu, K. L., & Sorooshian, S.  
755 (2020). The Atmospheric River-CONNECTed objeECT (AR-CONNECT) algorithm applied  
756 to the National Aeronautics and Space Administration (NASA) Modern-Era Retrospective  
757 Analysis for Research and Applications, Version 2 (MERRA V2) - 1983 to 2016. UC San  
758 Diego Library Digital Collections. <https://doi.org/10.6075/J0D21W00>
- 759 Shields, C. A., & Kiehl, J. T. (2016a). Atmospheric river landfall-latitude changes in future climate  
760 simulations. *Geophysical Research Letters*, 43(16), 8775-8782.  
761 doi:10.1002/2016gl070470

- 762 Shields, C. A., & Kiehl, J. T. (2016b). Simulating the Pineapple Express in the half degree  
763 Community Climate System Model, CCSM4. *Geophysical Research Letters*, *43*(14), 7767-  
764 7773. doi:10.1002/2016gl069476
- 765 Shields, C. A., Rutz, J. J., Leung, L. Y., Ralph, F. M., Wehner, M., Kawzenuk, B., . . . Nguyen, P.  
766 (2018). Atmospheric River Tracking Method Intercomparison Project (ARTMIP): project  
767 goals and experimental design. *Geoscientific Model Development*, *11*(6), 2455-2474.  
768 doi:10.5194/gmd-11-2455-2018
- 769 Spry, C. M., Kohfeld, K. E., Allen, D. M., Dunkley, D., & Lertzman, K. (2014). Characterizing  
770 Pineapple Express storms in the Lower Mainland of British Columbia, Canada. *Canadian*  
771 *Water Resources Journal*, *39*(3), 302-323. doi:10.1080/07011784.2014.942574
- 772 Stan, C., Straus, D. M., Frederiksen, J. S., Lin, H., Maloney, E. D., & Schumacher, C. (2017).  
773 Review of Tropical-Extratropical Teleconnections on Intraseasonal Time Scales. *Reviews*  
774 *of Geophysics*, *55*(4), 902-937. doi:10.1002/2016rg000538
- 775 Waliser, D. E., & Guan, B. (2017). Extreme winds and precipitation during landfall of atmospheric  
776 rivers. *Nature Geoscience*, *10*(3), 179-U183. doi:10.1038/Ngeo2894
- 777 Wheeler, M. C., & Hendon, H. H. (2004). An all-season real-time multivariate MJO index:  
778 Development of an index for monitoring and prediction. *Monthly Weather Review*, *132*(8),  
779 1917-1932. doi:Doi 10.1175/1520-0493(2004)132<1917:Aarmmi>2.0.Co;2
- 780 Williams, I. N., & Patricola, C. M. (2018). Diversity of ENSO Events Unified by Convective  
781 Threshold Sea Surface Temperature: A Nonlinear ENSO Index. *Geophysical Research*  
782 *Letters*, *45*(17), 9236-9244. doi:10.1029/2018gl079203

- 783 Zhou, Y., & Kim, H. (2017). Prediction of atmospheric rivers over the North Pacific and its  
784 connection to ENSO in the North American multi-model ensemble (NMME). *Climate*  
785 *Dynamics*. doi:10.1007/s00382-017-3973-6
- 786 Zhou, Y., & Kim, H. (2019). Impact of Distinct Origin Locations on the Life Cycles of Landfalling  
787 Atmospheric Rivers Over the U.S. West Coast. *Journal of Geophysical Research:*  
788 *Atmospheres*, 124(22), 11897-11909. doi:10.1029/2019jd031218
- 789 Zhou, Y., Kim, H., & Guan, B. (2018). Life Cycle of Atmospheric Rivers: Identification and  
790 Climatological Characteristics. *Journal of Geophysical Research-Atmospheres*, 123(22),  
791 12715-12725. doi:10.1029/2018jd029180
- 792 Zhu, Y., & Newell, R. E. (1994). Atmospheric Rivers and Bombs. *Geophysical Research Letters*,  
793 21(18), 1999-2002. doi:10.1029/94gl01710
- 794
- 795